Identification, Localization, and Quantification of Neuronal Cell Membrane Receptors with Plasmonic Probes: Role of Protein Kinase D1 in Their Distribution

6 **AUTHORS**, INCLUDING:

Lujan Masseroni
Instituto Nacional de Tecnología Agropecuaria
4 PUBLICATIONS **11** CITATIONS

SEE PROFILE

Ignacio Jausoro
National Scientific and Technical Research C…
9 PUBLICATIONS **121** CITATIONS

SEE PROFILE

Alberto M Díaz Añel
Instituto de Investigación Médica Mercedes …
11 PUBLICATIONS **302** CITATIONS

SEE PROFILE

Eduardo Andres Coronado
National University of Cordoba, Argentina
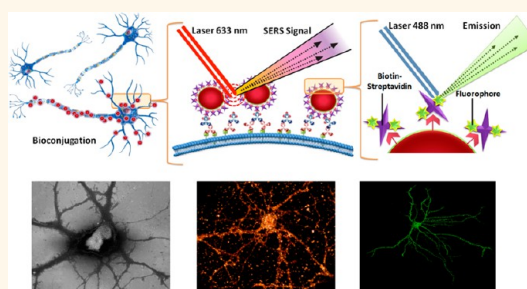**60** PUBLICATIONS **5,124** CITATIONS

SEE PROFILE

Identification, Localization, and Quantification of Neuronal Cell Membrane Receptors with Plasmonic Probes: Role of Protein Kinase D1 in Their Distribution

Juan C. Fraire,[†] M. Lujan Masseroni,[‡] Ignacio Jausoro,[‡] Eduardo M. Perassi,[†] Alberto M. Diaz Añel,[‡] and Eduardo A. Coronado[†,*]

[†]INFIQC, Centro Laser de Ciencias Moleculares, Departamento de Fisicoquímica, Facultad de Ciencias Químicas, and [‡]INIMEC, Laboratorio de Neurobiología, Universidad Nacional de Córdoba, Córdoba, 5000, Argentina. J. C. Fraire and M. L. Masseroni contributed equally to this work.

ABSTRACT Detecting, imaging, and being able to localize the distribution of several cell membrane receptors on a single neuron are very important topics in neuroscience research. In the present work, the distribution of metabotropic glutamate receptor 1a (mGluR1a) density on neuron cells on subcellular length scales is determined by evaluating the role played by protein kinase D1 (PKD1) in the trafficking of membrane proteins, comparing the distribution of mGluR1a in experiments performed in endogenous PKD1 expression with those in the presence of kinase-inactive protein kinase D1 (PKD1-kd). The localization, distribution, and density of cell surface mGluR1a were evaluated using 90 nm diameter Au nanoparticle (NP) probes specifically functionalized with a high-affinity and multivalent labeling function, which allows not only imaging NPs where this receptor is present but also quantifying by optical means the NP density. This is so because the NP generates a density (ρ)-dependent SERS response that facilitated a spatial mapping of the mGluR1a density distribution on subcellular length scales (dendrites and axons) in an optical microscope. The measured ρ values were found to be significantly higher on dendrites than on axons for endogenous PKD1, while an increase of ρ on axons was observed when PKD1 is altered. The spatial distribution of the NP immunolabels through scanning electron microscopy (SEM) confirmed the results obtained by fluorescence bright-field analysis and dark-field spectroscopy and provided additional structural details. In addition, it is shown using electrodynamic simulations that SERS spectroscopy could be a very sensitive tool for the spatial mapping of cell membrane receptors on subcellular length scales, as SERS signals are almost linearly dependent on NP density and therefore give indirect information on the distribution of cell membrane proteins. This result is important since the calibration of the ρ-dependent near-field enhancement of the Au immunolabels through correlation of SERS and SEM paves the way toward quantitative immunolabeling studies of cell membrane proteins involved in neuron polarity. From the molecular biology point of view, this study shows that in cultured hippocampal pyramidal cells mGluR1a is predominantly transported to dendrites and excluded from axons. Expression of kinase-inactive protein kinase D1 (PKD1-kd) dramatically and selectively alters the intracellular trafficking and membrane delivery of mGluR1a-containing vesicles.

Noble metal nanoparticle (NP) aggregates have long been recognized for their unique optical properties, particularly their capability to couple to each other through near- and far-field interactions. This feature gives rise to a variety of interesting optical phenomena extensively used in ultrasensitive spectroscopy and in the emerging field of biospectroscopy.[1] In addition, their surface properties allowed developing several functionalization strategies involving biomolecules, which have the capability of being specific linkers and also biorecognition agents able to preferentially interact with target molecules. In this respect, some proteins are an excellent choice to functionalize metal NPs since they are stable in aqueous solutions, can be readily

manipulated and further functionalized, and can also serve as linkers to construct nanoscale architectures with precisely controlled gaps between NPs.[2] As a result, they have the advantage that the distance and strength of the interaction between the nanocomponents in the resulting nanostructures can be precisely controlled using biomolecule-directed strategies.[3] The most exciting feature of using these kinds of nanostructures (biomolecule-functionalized NPs) in the emerging areas of biotechnology and biospectroscopy is the possibility to detect events and processes in biological systems with unprecedented levels of sensitivity and localization.[4,5]

One of the most interesting applications of functionalized plasmonic NPs is the characterization, detection, and quantification of cell membrane receptors. This information requires approaches that can probe the spatial organization of cell surface receptors on subdiffraction limit length scales,[6−16] which is a capability that is beyond those of the classical biomarker detection methods (e.g., flow cytometry). In that sense, based on immunolabeling and immunoassay techniques, which provide information on a single biomolecule within a cell, the optical plasmonic properties of gold and silver nanoparticles can be used to obtain information on receptor expressions in cell membranes through Raman and Rayleigh spectroscopy.[7,16−18] These techniques, surface-enhanced Raman spectroscopy (SERS) and Rayleigh spectroscopy, are one of the most exciting areas in biospectroscopy today. One example that has been used for several decades with applications in immunohistochemistry, immunoblotting, and immunoassay techniques is the use of immunological antibodies conjugated to colloidal gold particles for the detection of specific epitopes.[19−22] This antibody−Au nanospheres (NS) system allows the direct visualization of the gold nanoparticles through electron and dark-field microscopy, giving rise to new strategies besides the commonly used immunolabeling technique to investigate receptor density distributions in an electron microscope and in a common light microscope with a dark-field condensor.[23−26] In these techniques, the spatial distribution of the NP labels is used to obtain information about the local concentration of the targeted receptor.

The optical properties of plasmonic NPs are determined by coherent collective electron oscillations, the so-called localized surface plasmon resonances (LSPRs), which induce an enhanced electromagnetic field surrounding the metallic nanostructure with a spatial distribution that depends on its geometry, its orientation with respect to the incident polarization, illumination wavelength, and dielectric environment. In addition, the LSPR frequencies can be tuned by changing geometrical parameters, such as nanoparticle size,[27] shape,[27,28] crystal face,[29] surface roughness,[30] and interparticle spacing.[31−36] In that sense, if two or more NPs approach each other to within approximately one particle diameter on the cell surface, the oscillating E-fields surrounding the NPs interfere and induce a hybridization of the plasmon modes of the individual NPs.[37,38] According to this, the degree of enhancement in SERS spectra and the peak frequencies in the scattering spectra obtained with dark-field techniques are also determined by the shape, size, density, and proximity of the nanoparticles. Due to the distance-dependent electromagnetic interactions between Au NPs, the light scattered and the electromagnetic field enhancements achieved have been proposed to give indirect information about the local two-dimensional NP density (under optimum conditions, the signal amplification in SERS spectra and the frequency of the scattering spectra can be related directly to clustering of cell surface receptors). In this respect, the Reinhard group has recently shown that the density-dependent spectral response of 40 nm Au nanoparticle immunolabels targeted at specific receptors provides an alternative, nonfluorescence-based, optical approach for mapping the spatial distribution of receptor densities on cellular surfaces.[7,16] In some cases, however, it is not possible to obtain the scattering spectra of the NPs on the cell surface without interference of the scattering signal of the cell itself.

In this work we propose a functionalization strategy that allows evaluating the distribution of cell membrane receptors using simultaneously different techniques that allow obtaining qualitative and quantitative information on parameters of paramount importance in cell biology. The immunolabeling method was designed in order to achieve different kinds of information using the same plasmonic probe. The probe consist of 90 nm Au NSs functionalized by the addition of biotin simultaneously with the protein streptavidin (STV) (molar ratio biotin/STV 1:1). The biotin−STV complexes get chemisorbed onto the surface of the NSs and were added in a concentration ratio high enough to guarantee the presence of several STV molecules per NS. The three left unoccupied sites of the STV molecules can interact with specific biotinylated antibodies as in common immunolabeling techniques. Particularly, the STV molecules used in this work are conjugated with Alexa Fluor 488 dye molecules (STV_{488}), which allows one to perform in a simultaneous way also fluorescent imaging techniques such as fluorescence brightness analysis to map the spatial distribution of receptors on the cell membrane. These biotin−STV_{488}−bioconjugated Au NSs were applied to study a specific biological system that will be detailed below, although the methodology can be extrapolated to other biological studies.

The biological system selected in this work is neuron cells, which are highly polarized cells typically extending several short, thick, tapering dendrites and one functional, distinct, long, thin axon (see Scheme 1A).
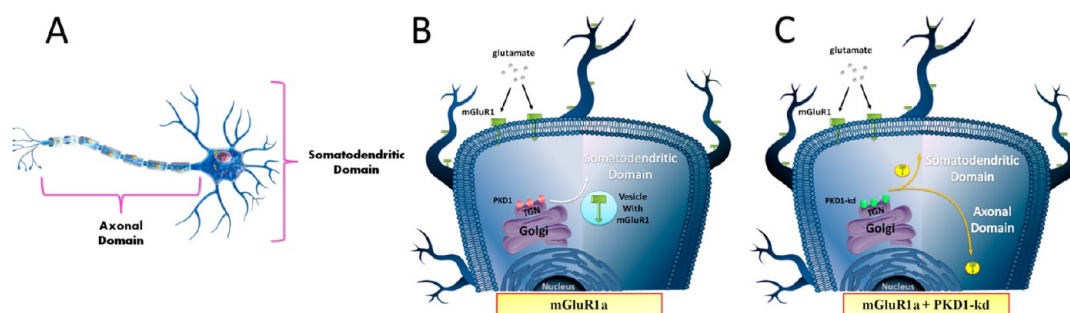
Scheme 1. Role played by PKD1 and PKD1-kd in regulating trafficking of dendritic membrane proteins in neuron cells. (A) Schematic representation of a typical neuronal cell (not in culture). Neurons are highly polarized cells typically extending several short, thick, tapering dendrites and one functional, distinct, long, thin axon (these domains are highlighted in the scheme). (B) Schematic representation of the effect of endogenous PKD1 expression in the distribution of mGluR1a receptors. The trafficking occurs mainly to somatodendritic domains. (C) Schematic representation of the effect of ectopic PKD1-kd expression in the distribution of mGluR1a. The expression of mutant PKD1-kd induces an alteration in the mGluR1a somatodendritic distribution, generating a homogeneous distribution among neuronal domains (dendrites and axons). This image is a modification of QIAGEN's original, copyrighted image by J. C. Fraire. The original image may be found at www.QIAGEN.com.

Consistent with this, many membrane proteins (cell membrane receptors) are preferentially distributed either to axons or dendrites, and neurons use different mechanisms to achieve this goal. The experiments described in this study were performed using neuronal cultures prepared from rat embryonic hippocampus, because this model system has been extensively used for studies of neuronal membrane protein trafficking. In particular, we have analyzed the involvement of protein kinase D1 (PKD1) in regulating trafficking of dendritic membrane proteins. PKD1, formerly called protein kinase Cμ (PKCμ), is a member of a family of dyacylglycerol (DAG)-binding serine/threonine kinases,[39] which also includes PKD2 and PKD3 isoforms. These kinases can be activated by diverse stimuli through PKC-dependent pathways[40,41] and have been implicated in diverse cellular functions.[41−45] During the past decade, PKD1 was described as a regulator for Golgi to cell surface directed trafficking.[39,42,46,47] Moreover, ectopic expression of PKD1 kinase-defective (PKD1-kd) mutants are shown to inhibit a specific membrane fission pathway involved in the transport of cargo proteins that contain basolateral sorting signals in MDCK cells,[48] suggesting that the formation of a trans-Golgi network (TGN) of cell surface specific transport carriers is regulated by PKD1-dependent fission pathways. In the specific cell type used in the experiments of this work (embryonic rat hippocampal pyramidal neurons), PKD1 was shown to have a key role in neuronal polarity, since the inactivation of this kinase selectively alters the intracellular sorting of specific postsynaptic somatodendritic membrane proteins, such as transferrin receptor (TfR) and the low-density receptor-related protein (LRP1), which in these conditions where retained at the axonal membrane.[49] These results indicate that in the absence of PKD1 missorting of dendritic membrane proteins important for regulating outgrowth (*i.e.*, neurotrophin or neurotransmitter receptors) would occur. In that sense, the target receptor chosen in this study is the metabotropic glutamate receptor 1a

(mGluR1a), which is an excitatory G-protein-coupled neurotransmitter receptor that is mainly expressed in the postsynaptic somatodendritic region of central nervous system neurons.[50] The neurotransmitter L-glutamate acts as the physiological agonist of mGluR1, activating mainly through this receptor a Gq/Phospholipase C-dependent pathway that leads to the release of calcium from inositol triphosphate (IP3)-dependent intracellular Ca^{2+} stores, a secondary messenger essential for numerous processes such as synaptic plasticity and neuronal degeneration and development.[51] Deficiencies in glutamatergic transmission have been associated with several neurological and neurodegenerative diseases such as ischemia, brain trauma, epilepsy, multiple sclerosis, amyotrophic lateral sclerosis, and Huntington and Parkinson diseases.[52,53] The precise role of this type of receptor in the mentioned diseases remains to be elucidated.[52] In the case of ischemia, differential effects of the activation of mGluR1 or mGluR5 (which could be affected by its inaccurate localization) might be responsible for the selective susceptibility to excitotoxic damage (a distinctive characteristic of ischemia) observed in the striatum.[54]

In this work we have evaluated the somatodendritic and axonal distribution of mGluR1a, both in normal endogenous PKD1 expression (control experiments) and PKD1-kd ectopic expression conditions (see Scheme 1B and C, respectively), through different light (fluorescence brightness analysis and SERS) and electron microscopy techniques (SEM). We demonstrate that SERS signals of reporter molecules between the NPs immunolabeled on a specific cell surface receptor facilitate a quantitative characterization not only of its surface expression but also of its spatial organization into cell domains (dendrites and axons). Our approach is based on the fact that at constant ambient refractive index the optical properties of NP immunolabels targeted to specific cell surface receptors depend both on the average separation and on the geometric
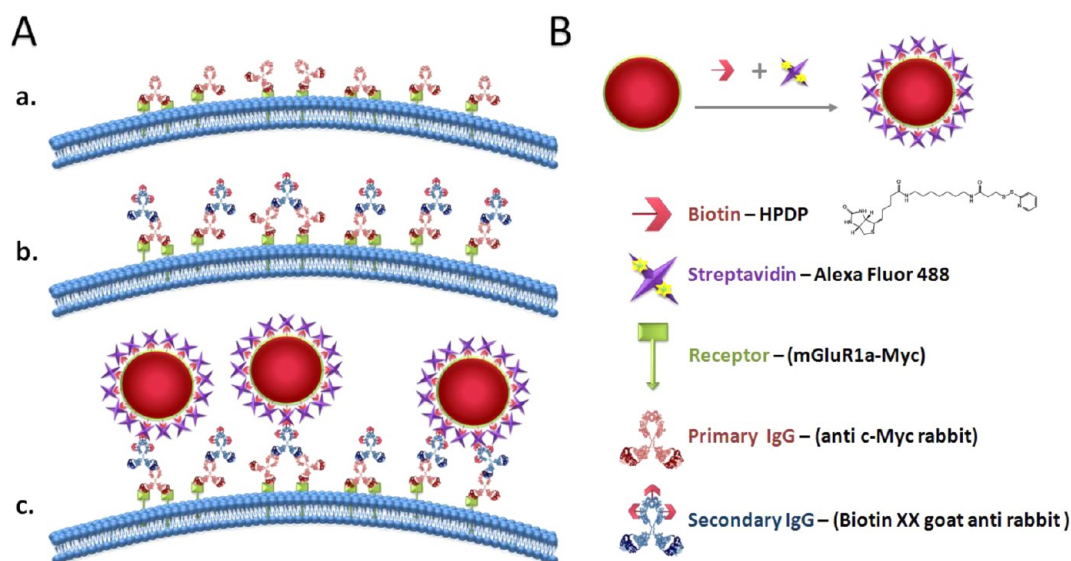
Scheme 2. Synthetic scheme showing the immunolabeling strategy onto cell surface receptors and the NP functionalization strategy. (A) Multivalent immunolabeling strategy for the detection of cell surface mGluR1a receptors. Primary anti c-Myc antibodies are bound to the receptors (a). Biotinylated secondary antibodies are anchored to the primary antibodies (b). The biotinylated antibodies carry multiple biotins to amplify the binding affinity of streptavidin-functionalized Au NPs in the last step (c). (B) NP functionalization strategy by biotin—STV. Biotin—STV—bioconjugated Au NSs are bound through the unoccupied biotin-binding sites of the STV proteins attached to the Au NSs.

arrangement of the NPs on the cell surface and, therefore, on factors that are determined by the underlying 2D spatial distribution of the targeted receptors. Previous studies had demonstrated that, due to the spectral shift in the spectrum of the scattered light, the near-field interactions between NP immunolabels at high density of immunolabeled NPs can be detected using conventional far-field optics,[7,9,10,12,16,54,55] but to the best of our knowledge no direct relationship between the SERS response of a reporter molecule and the quantification of a cell membrane receptor has been reported before.

We also perform electromagnetic simulations in order to understand the density dependence of the enhancement response of biomolecule-functionalized NPs targeted at mGluR1a cell surface receptors. The understanding of the combined effect of average NP density and spatial organization on the near-field properties of the bound NP immunolabels facilitates the experimental investigation of the cell/receptor system. In that sense, we quantify the relationship between the electromagnetic field enhancement factor and the NPs' density for 90 nm diameter Au nanosphere immunolabels targeted at mGluR1a receptors on neuron cells. We demonstrate through this relationship that SERS signals of reporter molecules enable a quantitative characterization of receptor densities on subcellular length scales through optical spectroscopy.

RESULTS AND DISCUSSION

Functionalization of the Plasmonic Nanoparticle Probes. The main objective of this study is the spatial mapping of the mGluR1a density on different neuron membrane domains (dendrites and axon). The visualization of the mGluR1a density either by optical or electronic techniques with metal NS immunolabels requires functionalized noble metal NPs that are stable against agglomeration in solution and that bind with high affinity selectively to their receptor target. In that sense, we designed a NS functionalization strategy based on the following points: (a) the high specific biomolecular recognition of STV with biotin, (b) the strong interaction energy of the STV—biotin system, and (c) the use of a rigorous stoichiometric control over the number of biotin molecules per STV molecule (molar ratio biotin/STV 1:1). This rigorous stoichiometric control is necessary due to the fact that STV molecules have four biotin-recognition sites, and more than one biotin per STV molecule could lead to NP agglomeration.[3] Therefore, we have employed an end-functionalized biotin (biotin HPDP) that facilitates a covalent attachment to the NP surface (biotin acts like a "glue" for the STV molecules). The biotin—STV complexes were added in a concentration ratio high enough to guarantee the presence of several STV molecules per NP (ratio STV/NPs 90 000:1). The three remaining unoccupied sites of the STV molecules can interact with specific secondary biotinylated antibodies, introducing an additional structural flexibility in the attachment chemistry to the membrane receptor and also amplifying the number of binding sites.

The labeling sequence is presented in Scheme 2. In the first labeling step a polyclonal anti-C-Myc antibody is attached to the Myc sequence of the mGluR1a receptors. This primary antibody is subsequently targeted by a biotinylated secondary antibody. In the last

A

B
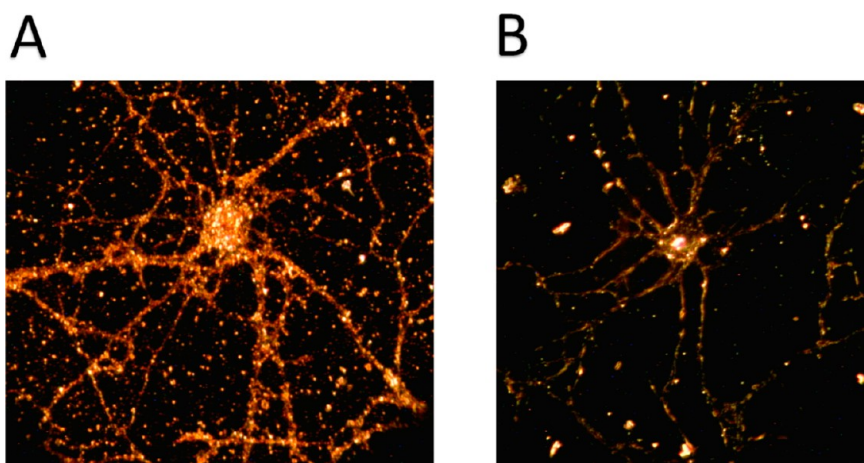
Figure 1. Dark-field image of a neuron cell with Au immunolabels using the labeling strategy outlined in Scheme 2. (A) Specific binding of functionalized Au NPs to the cell surface, leading to a vivid orange color. (B) Control experiment, where the labeling procedure was performed without using biotinylated secondary antibodies, which denotes only scattering of the cell surface. The absence of biotinylated antibodies rejects the possibility that functionalized Au NPs are bound to the specific target.

step biotin−STV−bioconjugated Au NSs are bound through the unoccupied biotin-binding sites of the STV proteins attached to the Au NSs. It is important to note that the number of NP labels bound to the cell surface after a constant incubation time depends on the NP concentration in solution, the number of receptors on the cell surface, and the binding affinity of the NP labels.

The strict stoichiometric control is necessary due to the ability of STV protein to interact with a maximum of four biotin molecules, which could induce the formation of NS aggregates.[3] According to this, the functionalization of 90 nm Au NSs was performed by the addition of biotin simultaneously with the STV protein in equal final concentrations (ratio STV/biotin 1:1). The high kinetic and thermodynamic constants of biotin−STV interactions guarantee the formation of biotin−STV complexes, avoiding a primary chemisorption of biotin molecules onto the NS surface, which could lead to the formation of NS aggregates (the interaction of the biotinylated NSs leads to the formation of random aggregates through H-bonds between biotins).[3,56]

The far-field optical and morphological characterization of 90 nm Au NSs' and functionalized NSs' stability is shown in Figure S1 in the Supporting Information. We monitored the UV−vis spectrum of a solution of functionalized NSs at 4.36×10^9 NSs/cm^3 (7.24×10^{-12} M) concentration over a time course of 2 h (Figure S1B). The extinction spectrum did not exhibit any significant spectral shift, which confirms that the particles were stable over time.

Dark-Field Optical Imaging of the Neural Cells with Au NS Immunolabels. Figure 1A and B compare a representative dark-field image of a fixed neuron cell stained with 90 nm Au immunolabels with a control neuron, obtained in the absence of Au immunolabels, respectively.

A simple eye inspection shows clear differences between control cells and the investigated NP-labeled cell. The neurons in the presence of Au NS immunolabels exhibit an intense orange color due to NPs bound to the cell membrane, while the control cell shows only the scattered light inherent to the cell.

The experimental scattering spectra of the functionalized NPs used as immunolabels as well as the electrodynamic simulation of the scattering spectrum of 90 nm Au NSs are available in Figure 2A. As can be seen in the figure, there are three different populations of particles that scatter in the green ($\lambda = 540$ nm), orange ($\lambda = 600$ nm), and red ($\lambda = 620$ nm). In order to explain this behavior, electrodynamic simulations of isolated 90 nm Au NSs and dimers with 10 nm and 20 nm gaps were performed. The simulations demonstrate that the scattering spectra of coupled particles red shift and increase in intensity with respect to the isolated particle. In that sense, the orange color observed in neurons with immunolabeled Au NSs could be attributed mainly to the presence of coupled NSs on the surface of the neuron cell (isolated particles scatter green and coupled particles scatter red). According to this, a better identification of functionalized neuron cells could be performed using a filter that only allows observing scattering for $\lambda > 633$ nm, which is attributed to the presence of coupled NSs. A representative dark-field image obtained with the filter of control neuron cells obtained in the absence of Au immunolabels is shown in Figure 2B, and dark-field images obtained with the filter of neuron cells stained with 90 nm Au immunolabels are shown in Figure 2C and D. As can be seen, nonfunctionalized cells present red scattering but only in the soma, with the dendrites and the axon being virtually indistinguishable in the black background (see Figure 2B). The same occurs with cells not transfected (with no overexpression of the cell
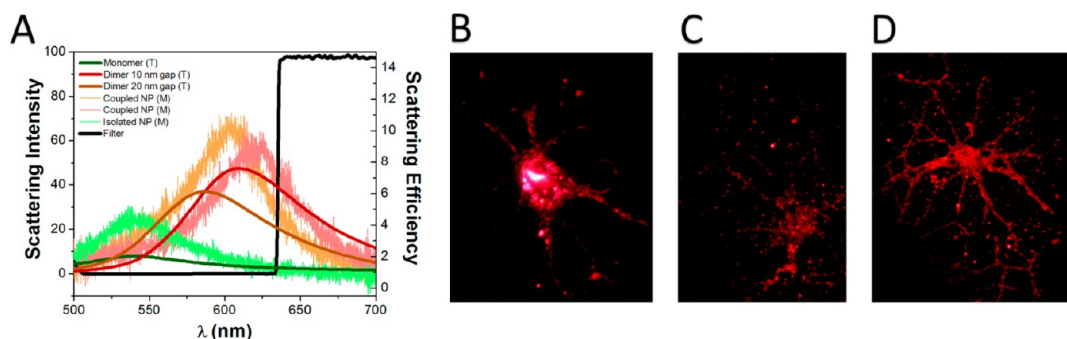
Figure 2. Distinguishing transfected neurons from nontransfected ones using dark-field microscopy. (A) Experimental scattering intensity of functionalized Au nanoparticles deposited onto a glass substrate (noisy lines) and the electrodynamic simulations of the scattering spectra of an isolated particle and dimers with 10 nm and 20 nm gaps (solid lines) that show a red shift of the maximum of the scattering spectrum as a function of the agglomeration of NPs. In the inset M denotes an experimental measurement and T denotes theoretical calculations. The black solid line represents the filter used to obtain the dark-field images of (B) a nonfunctionalized neuron cell (without adding nanoparticle probes), (C) a functionalized nontransfected neuron cell (adding nanoparticle probes to neurons with no overexpression of the cell membrane receptor), and (D) a functionalized transfected neuron cell (adding nanoparticle probes to neurons with overexpression of mGluR1a).

membrane receptor) with Au NS immunolabels, as the particles are not attached to the cell membrane through the specific immunolabeling, but only deposited in a nonspecific way (see Figure 2C). The fact that the same scattering as the nonfunctionalized cells is observed could be associated with the presence of isolated particles randomly distributed that scatter green light only. In contrast, transfected cells overexpress the cell membrane receptors recognized by the functionalized Au nanoparticles. This overexpression also occurs in other cell regions besides the soma (dendrites and axon), allowing visualizing dendrites and axons through the scattering of the Au nanoparticles attached in those regions (see Figure 2D).

As mentioned before, due to distance-dependent electromagnetic interactions between Au NPs, the light scattered has been proposed to give indirect information about the local two-dimensional NP density. This plasmon coupling microscopy has been proved to be a very interesting tool for mapping the spatial distribution of receptor densities on cellular surfaces.[7,16] Nevertheless, it is not always possible to obtain the scattering spectra of the NPs on the cell surface without interference of the scattering signal of the cell itself. This is the case for neuron cells, in which the cell scattering is of such magnitude that this direct correlation cannot be performed.

Although the optical images of the NP-labeled cells provide a quick survey of the relative functionalization and, therefore, of the expression of receptors on cell surfaces, it is difficult for this particular biological system to determine differences in receptor expression based only on the optical dark-field images.

Immunofluoresence Quantification of NS Immunolabel Densities. As mentioned before, the STV molecules used in this work are conjugated with Alexa Fluor 488 dyes (STV$_{488}$) that allow us to perform commonly used fluorescent imaging techniques such as fluorescence brightness analysis to map spatial distributions of receptors on the cell membrane. In order to quantify the fluorescence in axons and dendrites, several one-pixel-wide 100 μm lines were drawn on randomly selected portions of the axon and the dendrites (6−10 lines each), and the average fluorescence from each region was calculated. This average fluorescence from dendrites and axons for each experimental condition was calculated minimally from eight cells from at least three different cultures. The average values were corrected according to an average background fluorescence value determined from several regions containing unlabeled neurites.

The evaluation of the changes in the somatodendritic and axonal distribution of mGluR1a (missorting), in conditions of endogenous PKD1 or overexpression of PKD1-kd, is usually determined using a "polarity index" (PI) defined as

$$PI = \text{Dendrite Signal/Axon Signal} \qquad (1)$$

where "dendrite signal" and "axon signal" correspond, respectively, to any measurable parameter that can be used to infer the somatodendritic receptor density and the axonal receptor density. Uniform staining gives a PI value close to 1, whereas dendritic enrichment gives a value of >1, and axonal enrichment a PI value of <1.

We carried out preliminary experiments in order to compare the results using functionalized nanoparticles as specific probes for the cell membrane receptor with common immunofluorescence analysis. This control analysis consisted in the comparison of the average immunofluorescence brightness of cells using the labeling strategy mentioned above, i.e., a solution of Au NSs functionalized with a 1.2 × 10^{-7} M final concentration of STV$_{488}$ protein, with the average immunofluorescence brightness obtained for the incubation of cells treated with only STV$_{488}$ at the same concentration used to functionalize the nanoparticles. The comparison between both techniques was performed by the determination of the PI in the conditions of

normal endogenous PKD1 expression (see Figure S2 in the Supporting Information). The results show that using the functionalized nanoparticle technique, the same PI values as those obtained with common immunofluorescence analysis can be obtained. Once the validity of the functionalized nanoparticles method compared to common inmunofluerescence techniques was confirmed, we proceeded to determine the PI for the two experimental conditions of this work (*i.e.*, normal endogenous PKD1 expression and ectopic expression of PKD1-kd). The fluorescence images shown in Figure 3 reveal that in control experiments (normal endogenous PKD1 expression) the mGluR1a distribution occurs mainly on the somatodendritic domains, while in the ectopic PKD1-kd expression conditions mGluR1a missorting occurs, as evidenced by the PI decrease. This analysis clearly revealed that expression of mutant PKD1-kd induces an alteration in the mGlurR1a somatodendritic distribution, generating a homogeneous distribution among neuronal domains.

SEM Quantification of NS Immunolabel Densities. In order to verify the finding from our fluorescence brightness analyses, we inspected NP-labeled cell surfaces through SEM for normal endogenous PKD1 expression and ectopic PKD1-kd expression conditions, since the use of noble metal NPs to target the cell membrane receptors allows us to infer the spatial distribution of this receptor through direct observation of the particles in an electron microscope.

The quantification of NS immunolabel densities through inspection of the SEM images was determined by computing the average Au NS surface density (ρ), which was calculated using an image-processing program (Image-J). The average NP density for the different cell domains is a quantitative value that enables analyses of the expression levels of cell membrane receptors. The ρ values from dendrites and axons for each experimental condition were determined minimally from 10 cells from at least two different cultures. The average values were corrected according to an average background ρ value.

SEM micrographs of control cells are shown in Figure 4. The ρ values obtained were 51 NSs/μm^2 for dendrites and of 2 NSs/μm^2 for the axon. These values are clearly consistent with the SEM images of the dendrite and the axon, where a lower density of targeted NSs in the axon segment can be observed. In contrast, an inspection of the SEM micrographs of the ectopic PKD1-kd expression condition evidences an increase in the surface densities of NSs in the axon (see Figure 5). For this experimental condition the ρ values obtained were 30 NSs/μm^2 for dendrites and 8 NSs/μm^2 for the axon. The PI calculated according to the average surface densities is shown in Figure 6. The results obtained are in excellent agreement with those obtained for fluorescence brightness analysis
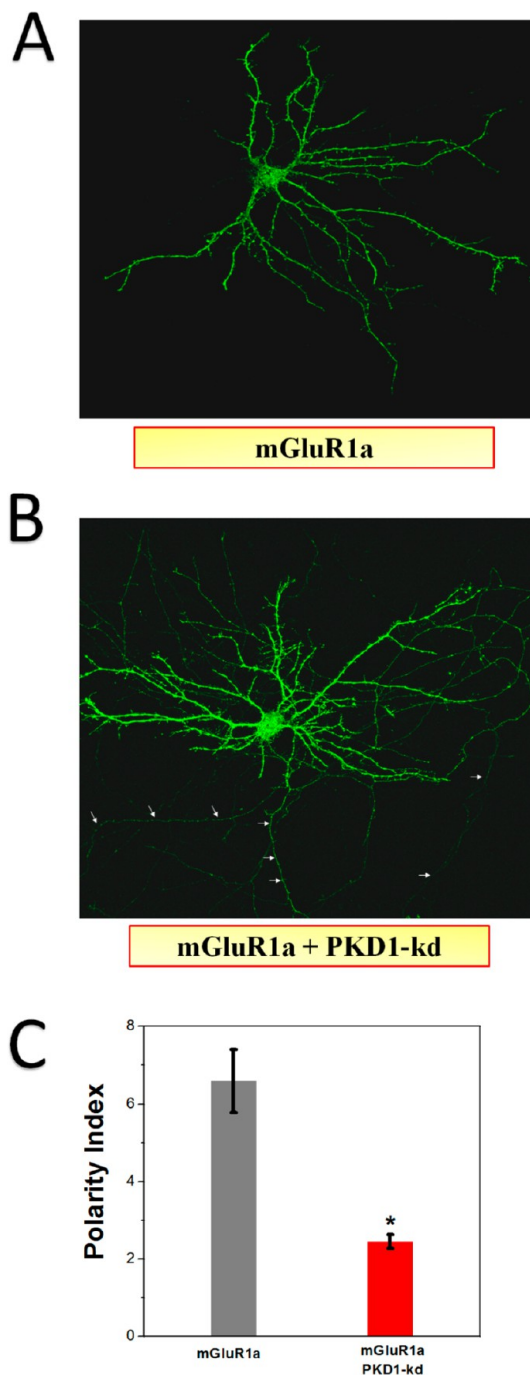
Figure 3. Quantification of NS immunolabel densities through immunofluoresence. (A) Confocal image showing the distribution of mGluR1a in a 10 d.i.v. hippocampal pyramidal neuron. Note that the distribution of mGluR1a is preferentially localized in the somatodendritic domain (the axon cannot be observed). (B) Confocal image showing the distribution of mGluR1a in an 8 d.i.v. hippocampal pyramidal neuron coexpressing PKD1-kd. Note that after coexpression of PKD1-kd, mGluR1a is localized in both the dendrites and axon (see the arrows in the figure). (C) Bar plot of the PI value calculated with average fluorescence intensities from neurons in the two conditions presented in this work: endogenous PKD1 (mGluR1a) and overexpression of PKD1-kd (mGluR1a + PKD1-kd). The values are the average ($\pm$SD, vertical bars) obtained for three separate experiments. The * represents significant differences according to Tukey's test ($p < 0.05$) for mGluR1a + PKD1-kd compared to mGluR1a.
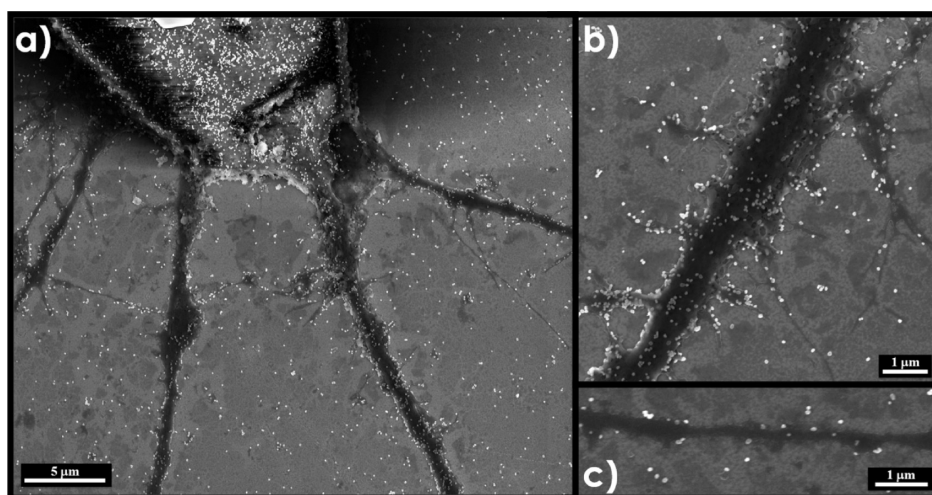
Figure 4. SEM images of Au NP-immunolabeled cells in conditions of endogenous PKD1 expression. (a) General view of NP distribution. (b) NP distribution on a dendrite. (c) NP distribution on an axon. Note that the NP density (ρ) is higher on dendrites (b) than on the axon (c).
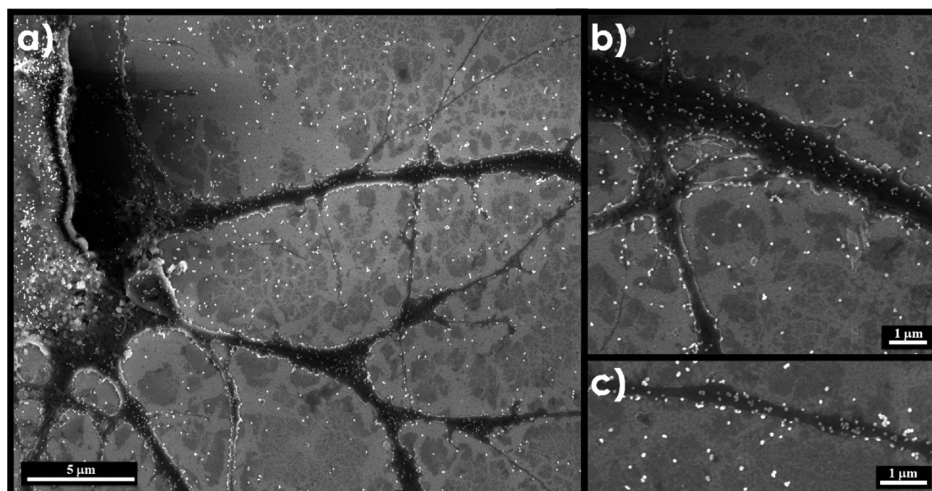

Figure 5. SEM images of Au NP-immunolabeled cells in conditions of ectopic expression of PKD1-kd. (a) General view of NP distribution. (b) NP distribution on a dendrite. (c) NP distribution on an axon. Note that the difference in NP density (ρ) on dendrites (b) and on the axon (c) is less significant than in the case of endogenous PKD1 expression.
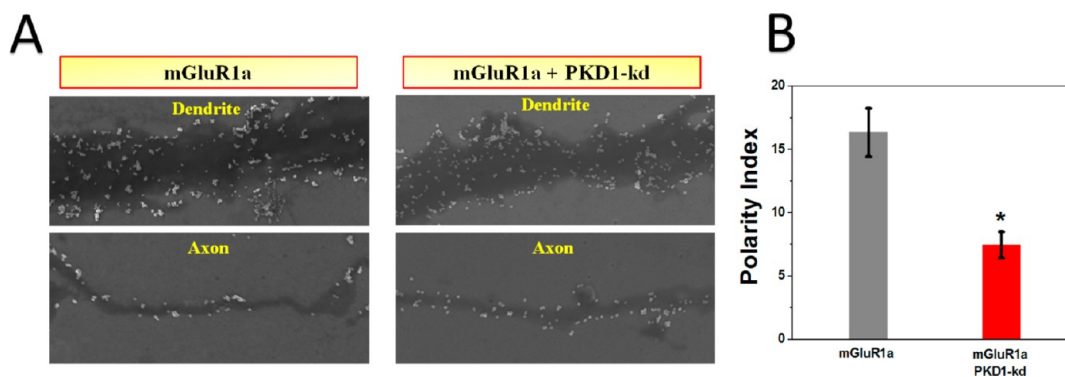
Figure 6. Quantification of NS immunolabel densities through SEM. (A) Representative SEM images of dendrites and axons for the two conditions studied: endogenous PKD1 expression (mGluR1a) and overexpression of PKD1-kd (mGluR1a + PKD1-kd). (B) Bar plot of the PI value calculated with average NP densities obtained by SEM. Values in B are the average ($\pm$SD, vertical bars) obtained for three separate experiments. The * represents significant differences according to Tukey's test ($p < 0.001$) for mGluR1a + PKD1-kd compared to mGluR1a.

(*i.e.*, ectopic expression of PKD1-kd induces missorting of the mGluR1a receptors).

It is important to note that the gold nanoparticle distribution shows that the antibody labeling is not uniform across the cell surfaces. Even this could be an effect of preferential clustering of the targeted receptors, as the size of the individual receptor accounts for less than 10% compared to the size of an individual NS, there is no direct correlation between the number of NPs and the number of mGluR1a receptors (see Figure S2A and B in the Supporting Information). Nevertheless, there are previous works that describe a preferential distribution of mGluR1a receptors into microdomains along the neuron cell membrane,[57] like those observed in the SEM images. Moreover, as discussed below, the preferential cluster formation of the NPs onto the cell surface has important implications in the electromagnetic field (E-field) enhancement responsible for the SERS spectra.

SERS Quantification of NS Immunolabel Densities. The primary aim of this section is to demonstrate that by using an immunolabeling protocol to attach gold nanoparticles to specific cell membrane receptors, it is possible to measure the SERS spectra corresponding to molecules in the hot spots between particles, and these SERS signals can be associated with the targeted-receptor density.

As mentioned above, the scattering spectrum of the cell membrane with NS immunolabels is dependent upon the NS density, and this feature has proved to be a valuable tool to quantify the degree of expression of the cell membrane receptors. Nevertheless, the complexity of the local environment of the 2D nanoparticle clusters in the cell membrane makes it very difficult to correlate the SERS signals to the receptor density, as one has to know, in principle, which is the Raman-active reporter (cell membrane components, functionalized molecules onto the nanoparticle surface, *etc*.). In that sense, in order to rationalize the experimental SERS response as a function of NSs density, careful experimental conditions have to be chosen (laser power) to guarantee that the SERS signal is free of background cell contributions, and also a rigorous wavenumber assignment of the vibrational modes of the SERS spectrum has to be performed to identify the Raman-active molecule.

The experimental SERS spectra were acquired from cells at 1% laser power and from NS-free cells at 1% (0.65 mW) and 100% (65 mW) laser power. This last condition (neuron cells without nanoparticles) gives rise to no discernible spectra at 1% laser power. On the contrary, a Raman cell spectrum was obtained at 100% laser power (see Figure S3 in the Supporting Information). Taking this into account, and to avoid spurious Raman signals coming from the cell, the lowest laser power was used. Under this condition, the presence of peaks in the SERS spectra can only be due to the presence of hot spots generated by NSs on the cell surface. Figure S4 of the Supporting Information shows the spectrum obtained from a dendrite of a neuron with endogenous PKD1 expression conditions. The wavenumber assignment was performed by deconvoluting the SERS spectrum to obtain the frequencies of the normal vibrational modes. This result was compared with the experimental frequencies of the vibrational modes from STV molecules obtained from ref 58. As can be observed, there is an excellent correlation between the reported experimental frequencies of the vibrational modes from the STV molecule and the deconvoluted frequencies of the SERS spectrum of the NS-labeled cells. This leads to the conclusion that by using this NS functionalization strategy the SERS spectra obtained can be directly associated with the functionalized molecules on the NS surface (STV protein), where signal intensity will strongly depend on the average separation and the geometric arrangement of the NPs on the cell surface and, therefore, on the underlying spatial distribution of the targeted receptors.

A quantitative determination of the mGluR1a distribution in the different cell domains for the two experimental conditions (endogenous PKD1 expression and ectopic expression of PKD1-kd) was computed by calculating the PI from the average SERS intensity obtained in axons and dendrites. This average was performed by measuring several spectra on randomly selected portions of the axon and the dendrites (10 points each) from 10 cells from at least two different cultures. The different relative NP densities of dendrites and the axon, revealed by the SEM images, as well as the SERS spectra of different spots on a neuron cell are presented in Figure 7A. As clearly observed, the maximum intensities of the SERS spectra are achieved in the dendrites where there is a higher NP density in comparison with the axon. In addition, although the peaks of the vibrational modes of STV are present in all the SERS spectra measured, the relative intensity of the vibrational modes is different from one spectrum to another. This could be due to heating effects associated with the LSPR excitation of the NSs at the excitation wavelength. This heating could give rise to vibrational excitation of the normal modes of the protein, leading to a conformational change of the protein located in the hot spots (*i.e.*, the vibrational excitation of the protein leads to a change of its conformation).[59] Therefore, to avoid errors inherent to the variation of the relative intensities of the different vibrational modes, the integral value of the SERS signal in the range $1650-1510$ cm^{-1} was calculated (see Figure 7B). This range of frequencies involves the amide I (absorbing near 1650 cm^{-1}, which arises mainly from the C=O stretching vibration with minor contributions from the out-of-phase C−N stretching vibration, the C−C−N deformation, and the N−H
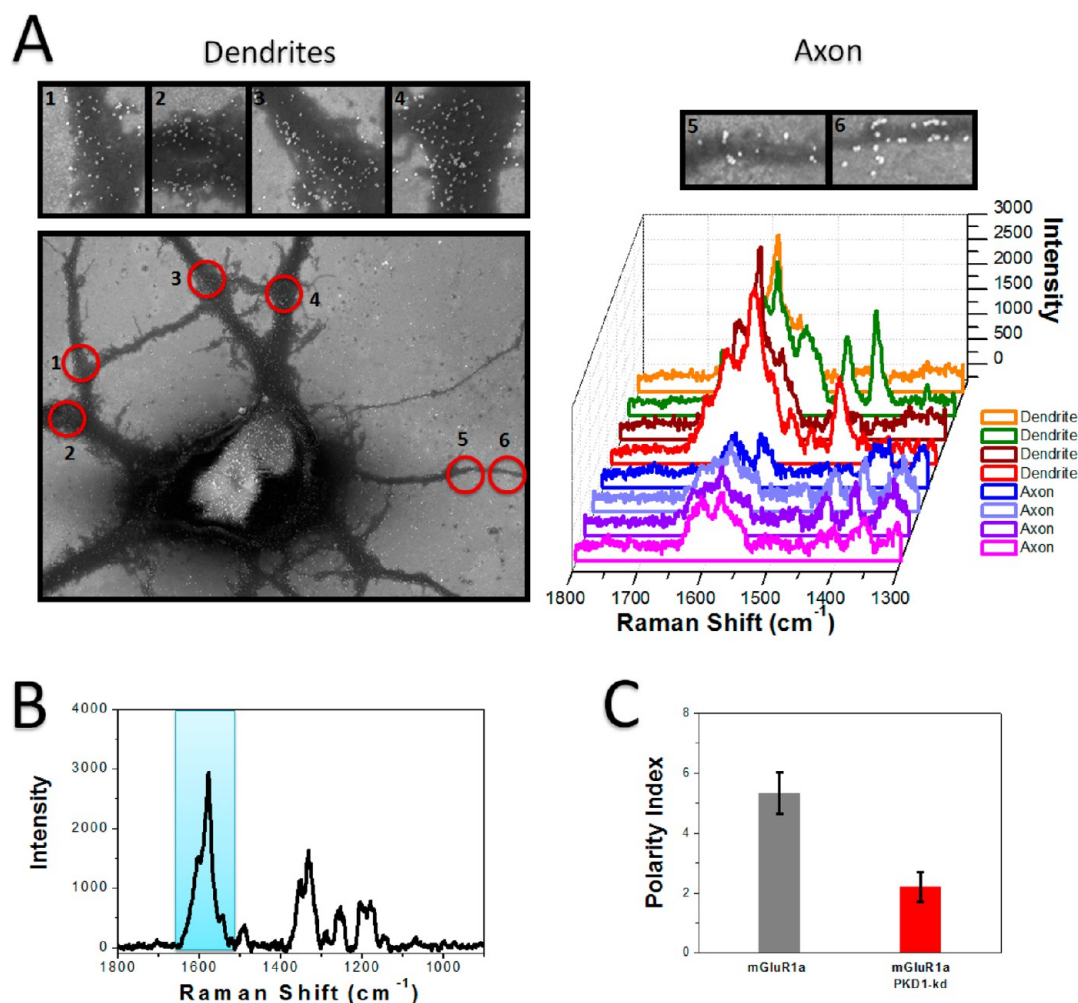
Figure 7. Quantification of NS immunolabel densities through SERS. (A) Comparative scheme showing the relative intensity changes of the SERS spectra as well as the relative densities obtained in the SEM images associated with the spectral changes in the subcellular protrusions of the neuron cell (dendrites and axon). **(B)** Schematic illustration of the selected frequency range for integration of the SERS signals. **(C)** Bar plot of the PI value calculated using the average SERS intensities for the two conditions studied: endogenous PKD1 expression (mGluR1a) and overexpression of PKD1-kd (mGluR1a + PKD1-kd). Values in C are the average (±SD, vertical bars) obtained for three separate experiments. The * represents significant differences according to Tukey's test ($p < 0.01$) for mGluR1a + PKD1-kd compared to mGluR1a.

in-plane bend) and the amide II (absorbing near 1510 cm^{-1}, which arises from the out-of-phase combination of the N–H in-plane bend and the C–N stretching vibration with smaller contributions from the C=O in-plane bend and the C–C and N–C stretching vibrations) normal vibrational modes of the STV protein.[60] The calculated PI using these SERS-integrated signals from dendrites and axons in the two experimental conditions of this work is shown in Figure 7C. The results not only are in very good agreement with those obtained through florescence and SEM analyses but also demonstrate the usefulness and sensitivity of SERS applied to the determination of cell surface receptor distribution with plasmonic nanoparticle probes.

Correlating the Spectral SERS Response with Electrodynamics Simulations (E-Field Enhancement–Density Relationship). The consistency between fluorescence, SEM, and SERS characterizations of the NP densities, and therefore

the mGluR1a receptor distribution, on dendrites and axons confirms that the SERS mapping due to plasmon coupling enables the detection of ρ differences on subcellular length scales. The elucidation of the underlying electromagnetic interaction mechanisms between the NPs on the cell surface and the NS density was performed by a session of calculations of the E-field enhancement increasing NP density. In this way, we were able to indirectly correlate the measured SERS with the immunolabel density on the cell surface.

The major contribution to the SERS signals comes from the electromagnetic enhancement caused by LSPR excitations. Another mechanism often argued to explain SERS is the chemical one, but this mechanism has proved to have by far a lower contribution[61] and alone cannot account for the 10^6–10^8 enhancements observed in many experiments. In addition, this mechanism is still the subject of considerable research work, but it is now accepted that it could

contribute with a factor of 10−100 to the global enhancement.[56,62]

The theoretical electromagnetic SERS enhancement, for small Raman shifts, scales with the fourth power of the field enhancement, while for Raman shifts that are significantly greater than the width of the plasmon resonance, local electromagnetic SERS enhancement scales with the product of the field intensity enhancements at the incident and scattered frequencies.[61] Considering that the fourth-power approximation is valid, the electromagnetic field enhancement factor (EFEF) is defined by

$$EFEF = |\Gamma(\omega)|^2 \qquad (2)$$

$$|\Gamma(\omega)| = \left(\left| \frac{E(\omega)}{E_0(\omega)} \right| \right)^2 \qquad (3)$$

where $|\Gamma(\omega)|$ is the square of the enhanced electric field generated at the frequency of the incident radiation (ω).

We will examine the variation of the EFEF with ρ, by rigorous electrodynamics modeling using generalized multiparticle Mie (GMM) theory. In all cases, the simulations were performed assuming an effective refractive index of nr = 1.23, which was estimated according to the effective medium approximation[63] as an average of the refractive indices of the membrane (nr =1.45) and the surrounding air (nr = 1.0003).

In order to evaluate the EFEF as a function of the NP density (EFEF(ρ)), 11 different densities (from 1 to 50 NSs/μm^2) and five different random configurations for each density were considered. In addition, the EFEF has been computed using various lower limits of the enhancement (Γ_{min}) to calculate the average:

$$\langle \Gamma(\omega) \rangle = \int_{\Gamma_{max}}^{\Gamma_{min}} \Gamma_i(\omega) \, di / \int_{\Gamma_{max}}^{\Gamma_{min}} di \qquad (4)$$

where i correspond to the ith point in the simulated grid. As expected, increasing the lower limit of integration (Γ_{min}), increases the value of the average EFEF. Although the regions of highest enhancement are achieved in the hot spots between closely interacting nanoparticles, the experimental SERS signals cannot be attributed only to those generated in these gaps (*i.e.*, strongly coupled nanoparticles with very small gaps between them). Taking into account this feature, a suitable lower limit should be considered. As evident, the average enhancement in eq 4 will strongly depend on the lower limit of the enhancement (Γ_{min}) used to perform the integration: the lower the limit of integration (Γ_{min}), the larger should be the value of $\langle \Gamma(\omega) \rangle$. As an example, Figure S5 (in the Supporting Information) maps the regions with enhancements greater than a certain minimum enhancement value (Γ_{min}). The different colors used in this figure correspond to the different values of Γ_{min} (blue for $\Gamma_{min} = 9$, red for $\Gamma_{min} = 100$, and green for $\Gamma_{min} = 400$). This result clearly shows

that regions with $\Gamma \geq 9$ overestimate the interparticle regions considering regions of very poor coupling effects, while regions with $\Gamma \geq 400$ only consider extremely close nanoparticles, underestimating several active gaps. The regions with enhancements $\Gamma \geq 100$ suitably comprise nanoparticles close enough to each other that could give rise to interparticle gaps having significant enhancement factor values, comprising close and not so close nanoparticles within the sample in a more realistic fashion. Therefore, the Γ_{min} chosen for the EFEF calculations was $\Gamma \geq 100$. In Figure 8 we show the simulated near-field spatial distribution for different two-dimensional NP densities for selected ρ values ($\rho = 10, 20, 30, 40, 50$ NSs/μm^2, Figure 8A−E) and EFEF(ρ) relationships obtained for the random NS distribution across the entire investigated ρ range (Figure 8F). The EFEF(ρ) relationship of the random NS distribution shows a linear dependence on NS density at least in the ρ range investigated. Nevertheless, it is expected that as the number of NSs increases, this trend will reach an asymptotic regime, as all available sites for NSs should be occupied, giving rise to the maximum plasmon coupling between NPs.

In order to give a quantitative correlation between the simulations and the experimental SERS response, the PI was determined using the theoretical EFEF(ρ) relationship and the experimental ρ values obtained through SEM. The calculated PI is shown in Figure 9 together with the near-field simulation for the experimental ρ values obtained. At low ρ values the near-field response is dominated by individual, noninteracting NSs. Note that due to the random nature of our simulation, even at low ρ values, some interacting nanoparticles are present, but by choosing a suitable average value (*i.e.*, choosing an appropriate lower limit value of Γ to perform the average) this value is lower than at higher densities. As ρ increases, the probability of finding NSs at close enough distances increases as well, generating highly localized enhanced fields in the gaps (hot spots). On the other hand, the average number of hot spots between coupled NSs on the cell surface increases as well. As both effects go in the same direction, the overall effect is a net increase of the SERS response with ρ (see Figure 7 and Figure 8). At this point, it is important to consider one important issue. As observed in the SEM images, even at low NS densities, some degree of clustering of several NSs is present. This could be attributed to a heterogeneous distribution of mGluR1a on the neuron surface (microdomain distribution). In this case the average value of EFEF will depend not only on ρ but also on its spatial organization. Therefore, a preferential clustering of NS labels due to a heterogeneous receptor distribution into microdomains will lead to average EFEF values significantly higher compared to a homogeneous random NP distribution, even if the average ρ value is identical. The dependence of EFEF on both ρ
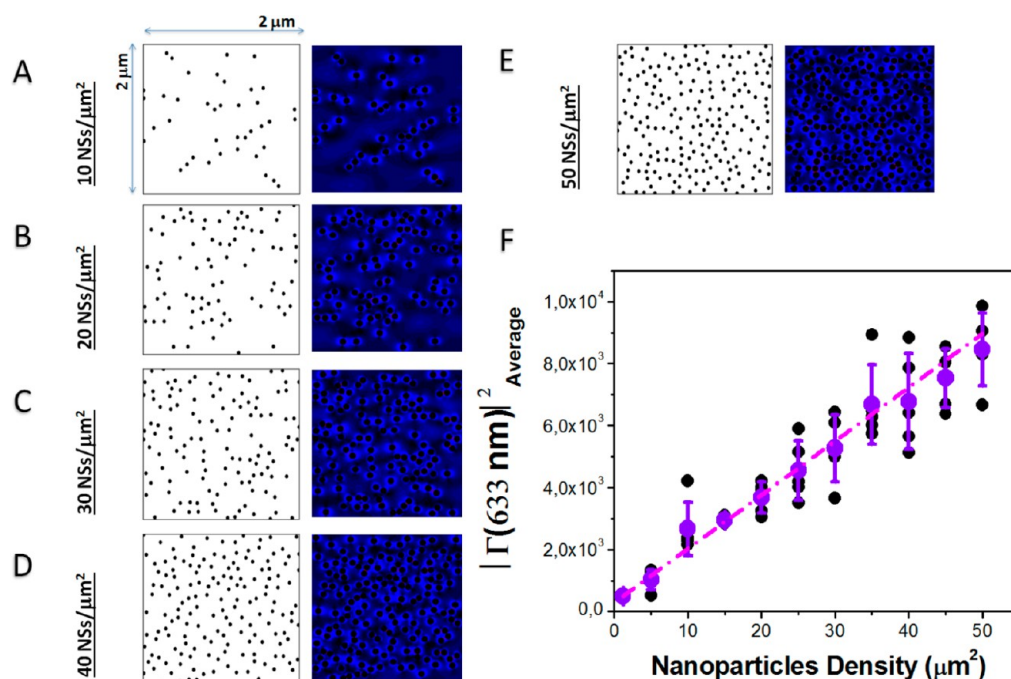
Figure 8. Simulated near-field response as a function of NP density irradiating at 633 nm. (A–E) Simulated near-field spatial distribution for different two-dimensional NP distributions for selected ρ values (ρ = 10, 20, 30, 40, 45 NSs/μm^2). (F) Relationship between the electromagnetic field enhancement factor (EFEF) and ρ. The relationship was determined for 11 different densities (from 1 to 50 NSs/μm^2) and five different random configurations for each density. The average EFEF(ρ)'s are presented in violet-colored circles.
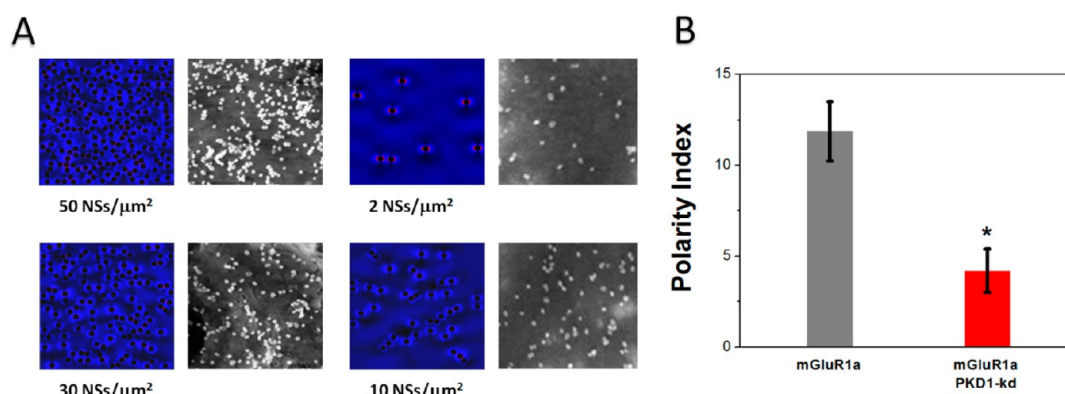

Figure 9. Quantitative correlation between NS immunolabel densities and theoretical near-field simulations. (A) Simulation of the near-field response of a random NP distribution and the experimental SEM image with almost identical NP density. (B) Bar plot of the PI value calculated using the EFEF(ρ) relationship and the experimental ρ values obtained through SEM, for the two conditions studied: endogenous PKD1 expression (mGluR1a) and overexpression of PKD1-kd (mGluR1a + PKD1-kd). Values in B are the average ($\pm$SD, vertical bars) obtained for three separate experiments. The * represents significant differences according to Tukey's test ($p < 0.05$) for mGluR1a + PKD1-kd compared to mGluR1a.

and the heterogeneity of the NP distribution could be directly related to the spatial organization of the cell membrane receptors.

As our simulations were performed in random distributions but introducing microdomain distribution with some degree of clustering, the PI determined by our simulations reproduces very closely the one determined for SEM and also the PI factor obtained by the SERS experiments. Under this condition, an increase in ρ leads to an increase in the number of strongly coupled NPs.

The very good agreement obtained for the PI factors using different techniques has been discussed here. In all cases, the results indicate that in endogenous PKD1 expression the distribution of the mGluR1a occurs preferentially in the somatodendritic domains of neuron cells, while in the presence of PKD1-kd missorting of this receptor to axonal domains occurs. A direct correlation between the results obtained by the different techniques is presented in Figure 10, where the ratio between the PI values obtained for the two different experimental conditions is directly
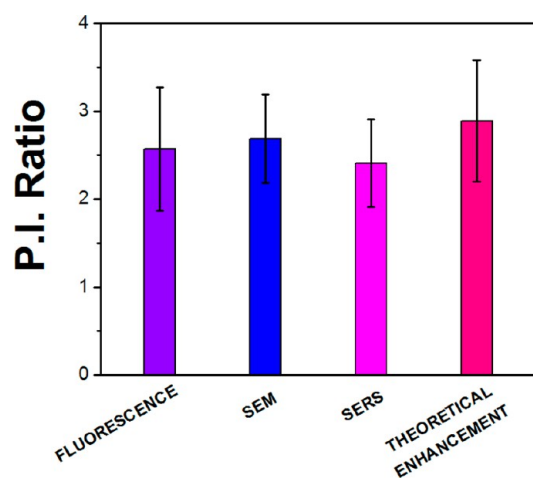
Figure 10. Bar plot showing the quantitative comparison of the PI ratio determined through fluorescence, SEM, SERS, and theoretical near-field simulations.

compared between each technique described in the article (PI ratio = PI of endogenous PKD1 expression/PI of ectopic PKD1-kd expression). As can be seen, there is an excellent correlation between all techniques, including the theoretically determined PI, with the theoretical values being only slightly higher. This difference can be rationalized if one considers that EFEF was calculated using several approximations where the substrate was only considered through the effective medium approximation instead of an explicit consideration, the fourth power approximation of the enhanced field, and also no NPs size dispersion was considered.

CONCLUSIONS

Using a multivalent labeling functionalization of Au NPs we achieved a highly efficient and selective labeling of a glutamate neurotransmitter receptor (mGluR1a). We evaluated the role of PKD1 in the trafficking of mGluR1a in neuron cells by the quantification of somatodendritic and axonal distribution, in both endogenous PKD1 expression and ectopic PKD1-kd expression conditions. Similar analyses to those performed for mGluR1a in this work will in the future be possible with different cell membrane receptors.

Compartmentalization in different domains is crucial to the proper functioning of neuronal cells. Both somatodendritic and axonal domains have their own pool of membrane proteins, which are classified in different sections of the secretory pathway to reach their correct final destination. It was established that alterations in dendritic or axonal protein sorting leads to substantial changes in the development of these neuronal compartments, as well as at the level of synaptic transmission, and hence to neuronal plasticity events associated with diverse diseases such as epilepsy and Huntington and Parkinson diseases, among others.

The results presented in this article suggest that in neurons PKD1 is involved in mGluR1a regulating distribution, probably at the TGN level. In that sense, it became evident that expression of PKD1-kd induces a dramatic alteration in the intracellular distribution of mGluR1a receptors. As expected, in control neurons (endogenous expression of PKD1) mGluR1a was predominantly restricted to the somatodendritic domain. In contrast, when neurons were transfected with PKD1-kd, mGluR1a was found not only in dendrites but also widely distributed along axons. This analysis clearly revealed that expression of PKD1-kd induces missorting. Thus, after expression of the kinase-inactive mutant of PKD1, selective trafficking of mGluR1a to dendrites and their delivery to the dendritic plasma membrane are completely altered. This could be explained as, after PKD1 inactivation, missorting occurs because of a defect in the biogenesis of normal vesicles at the Golgi with cargo entering the wrong vesicle.

We have demonstrated that SERS signals of reporter molecules between the NP immunolabeled to a specific cell surface receptor facilitate a quantitative characterization not only of its surface expression but also of its spatial organization into cell domains (dendrites and axons). Moreover, we showed by combining optical spectroscopy and electron microscopy, as well as through computational electromagnetic simulations, that the distance-dependent near-field interactions between NP immunolabels enable characterizing the average NP density on the cell surface on subcellular length scales.

We have performed a detailed analysis and discussion of how the EFEF relates with the NP density as well as on the spatial organization of the receptors on subdiffraction limit length scales. In the case of the mGluR1a the immunolabels were found to cluster on the cell surface even at low−medium NP densities, which is consistent with heterogeneous receptor distributions into microdomains. It was found that near-field simulations of the experimentally observed NP distributions as a function of ρ reproduced quite well the PI ratio determined experimentally by fluorescence, SEM, and SERS. In addition we further demonstrated that SERS response (dominated by STV molecules located in the hot spots) could also be used to infer the density of the targeted receptor. In the context of this work, we concluded that our combined experimental and theoretical studies confirm that the SERS responses of NP immunolabels targeted at cell surface receptors are able to provide information not only about relative expression levels but also about the preferential spatial organization of the receptors on the cell surface into clusters.

Certainly, for detection techniques based on the optical properties of the plasmonic nanoparticle probes, like SERS, the detection sensitivity for the quantification of cell surface molecules will be dependent upon the

near-field optical properties of NP immunolabels targeted to specific cell surface receptors and, therefore, on factors that are determined by the 2D underlying spatial distribution of the targeted receptors (*i.e.*, on the average separation and the geometric arrangement of the NPs on the cell surface). Receptors clustered into microdomains (*i.e.*, mGluR1a) are expected to give rise to smaller interparticle distances between the targeted NPs, increasing the number of hot spots and, as a consequence, producing higher field enhancements and therefore higher SERS intensity for a given mode. In the case of cell membrane receptors that present a homogeneous distribution, the average distance between receptors would be a crucial factor, which would be taken into account in order to give a realistic comparison between experimental intensity of the SERS signals and the EFEF as a function of the NP density (EFEF(ρ)). Nevertheless, this technique by itself cannot give enough information on the spatial distribution of the cell membrane receptors. A more direct correlation of the 2D underlying spatial distribution of the targeted receptors could be performed though SEM using nanoparticles with a size close to the size of the membrane receptor.

In summary, in the present work we have proposed a novel functionalization strategy that allows evaluating the distribution of cell membrane receptors using simultaneously different techniques that give not only qualitative but also quantitative information on parameters of paramount importance in cell biology. Moreover, we have demonstrated that the optical properties of NP immunolabels in combination with efficient labeling procedures enable the differentiation of relative expression levels of cell surface receptors (in this work mGluR1a) through different light (fluorescence brightness analysis and SERS) and electron microscopy (SEM) techniques. We further quantified the differences in the NP labeling between the investigated cell/receptor systems through spectral analysis of the collective plasmon resonance wavelength of the NP labels on the cell surface. A systematic characterization of the electromagnetic interactions (EFEF) between NP immunolabels confined to a two-dimensional cell surface revealed that the measured SERS response depends both on the average NP density and on the level of NP clustering on the cell surface.

MATERIALS AND METHODS

Materials. The following materials were used as obtained: HAuCl4 (Carlo Erba); sodium citrate (Mallinckrodt); EZ-Link biotin-HPDP (Pierce); streptavidin (Invitrogen); polyclonal anti c-Myc rabbit antibody (Santa Biotechnology, Inc., USA); anti-rabbit IgG biotin conjugate goat antibody (Molecular Probes, Inc., USA); Lipofectamine 2000 (Invitrogen, Carlsbad, CA); poly-L-lysine (Sigma, USA); neurobasal medium (Gibco); B27 (Gibco); N2 supplement (Gibco).

Au Nanosphere Synthesis. The synthesis of gold nanoparticles was performed using the Turkevich method, which is based on the reduction properties of boiling citrate solutions. Briefly, they were produced by reducing a 50 mL 0.2 mM chloroauric acid solution (HAuCl$_4$) with the addition of 0.5 mL of a 0.01 M citrate solution (corresponding to a 1:0.5 Au/citrate molar ratio) under heat and rapid stirring for 30 min. The morphological characterization of the Au NSs was performed combining UV–vis spectroscopy, TEM, dynamic light scattering (DLS), and electrodynamic modeling using Mie theory. The overall results after combining all of these different techniques and modeling indicate that the average diameter of Au NSs was 90 nm with a picomolar concentration of 4.36×10^9 NSs/cm^3 (7.24×10^{-12} M), estimated using the experimental extinction intensities at the maximum wavelength, and the cross section was calculated using Mie theory for spherical particles with a suitable diameter (determined by TEM).

Particle Funcionalization. EZ-Link biotin-HPDP (*N*-[6-(bio-tinamido)hexyl]-3′-(2′-pyridyldithio)propionamide) was used for surface modification of 90 nm Au NSs. The procedure for the functionalization of a 1 mL NS solution consists in incubating the colloidal dispersion using simultaneously EZ-Link biotin-HPDP and streptavidin (molar ratio NSs/biotin/STV 1 $\leq$ 1:1) for around 12 h at room temperature. The amount of biotin–streptavidin complex was high enough to guarantee a complete surface functionalization of biotin. The biotin–streptavidin-functionalized NSs were washed by centrifugation (4.500 rpm, 10 min) and resuspended in water.

Extinction Measurements. The characterization by UV–vis spectroscopy was carried out by scanning in the 200–1100 nm range. The spectra were measured using a Shimadzu UV-1700

PharmaSpec spectrophotometer with a 1 cm quartz cell at room temperature.

DLS Measurements. The characterization by dynamic light scattering was performed by recording the intensity of the scattered light as a function of the particle diameter in colloidal solutions. The samples were measured using a Delsa Nano 2.2 spectrometer with a 1 cm quartz cell at room temperature.

Transmission Electron Microscopy. Transmission electron microscopy (TEM) images were obtained using a JEM-JEOL 1120 EXII under an accelerating voltage of 80 kV. Samples were prepared by adding one drop ($\sim$50 μL) of the sample colloidal solution onto a holey carbon-Formvar coated copper TEM grid (100 mesh).

Cell Culture. Neuronal cultures from embryonic rat hippocampi were prepared as described previously.[64,65] Neurons [10 days *in vitro* (d.i.v.)] with long axons and well-developed dendritic arbors (stage 5) were used for all experiments. After transfection, neurons were fixed, blocked, and incubated with primary antibodies.

DNA Constructs and Transfection. GST-PKD1-kd (kinase dead) was a generous gift from Yusuke Maeda (Immunology Frontier Research Center, University of Osaka, Japan), and pJPA5-mGluR1a (FL)-Myc was a contribution from Dr. G. Banker. pJPA5-mGluR1a (FL)-Myc has a myc sequence in the NT domain; this feature is the main reason for detecting the receptor on the cell surface.

Transient transfection of cultured neurons was performed as described previously,[66] and the constructs were used at a concentration of 4–10 μg/μL unless otherwise stated.

Immunolabeling and Sample Preparation for Optical Studies. Neuron cells were fixed by immersion in a 4% formaldehyde solution in 4% sucrose containing PBS for 20 min at room temperature. The cells were then washed three times by immersion into ice-cold 1$\times$ PBS for 5 min each time. The fixed cells were then incubated in ice-cold 1$\times$ PBS buffer containing 1% BSA for 1 h at room temperature to block nonspecific binding. After that, the cells were washed again three times with ice-cold 1$\times$ PBS for 5 min each. The cell slides were then incubated with polyclonal anti c-Myc rabbit (diluted 1:350 in 1$\times$ PBS) for 1 h at RT. The cells were subsequently washed three times with ice-cold 1$\times$ PBS for

5 min each. In a subsequent step, biotin-labeled secondary IgG goat anti-rabbit antibody (diluted 1:300 in 1× PBS) was incubated with the above cell slides for 1 h at RT. Then the cells were again washed three times with ice-cold 1× PBS for 5 min each. In the subsequent immunolabeling step, each cell slide was covered with 100 μL of biotin−streptavidin (1:1)-functionalized Au NPs for 3 h at RT in a water vapor saturated atmosphere and then washed with ice-cold 1× PBS three times for 5 min. The cell slides were then integrated into a montage medium (Fluorosave, Calbiochem).

Preparation of SEM Samples. The culture and immunolabeling procedures for SEM were identical to those used for sample preparation in the optical studies with the exception that the neuron cells were grown on silicon substrates. After immunolabeling, the silicon substrates were washed twice with ice-cold 1× PBS and then briefly immersed into ddi water to remove the salt on the surface.

Dark-Field Microscopy. We used a dual microscope (Olympus BX51), which combines transmitted and reflected light microscopes. The microscope was modified in order to introduce dark-field condensers.

For experiments, an Olympus air dark-field condenser (NA = 0.92−0.8), an Olympus objective LPlan 100× (NA = 0.70), an Olympus objective SLMPlan 50× (NA = 0.45), an edge 633 nm filter, and a halogen lamp of the microscope were used. An Angstrom Sun CFM-USB-4 1280 × 1008 pixels camera, which is attached to the microscope, allows us to record images of the cells.

Rayleigh Spectroscopy. Rayleigh scattering spectra were measured using a Horiba LabRaM HR800 spectrometer coupled to a dark-field microscope. A 600 lines nm^{-1} grating and a Synapse CCD 1024 × 256 detector, which are included in the Horiba LabRaM, allow the collection of the Rayleigh scattering signals. LabSpec 5 software is used to record the Rayleigh scattering spectra. The spectra were corrected according to background and to the excitation source spectrum.

Confocal Fluorescence. Fluorescence images were obtained using a confocal (Zeiss Pascal) microscope fitted with a 40×, 1.4 NA objective. The excitation wavelength used was 488 nm (laser line from an argon laser). Images were processed using Adobe Photoshop.

Scanning Electron Microscopy. Scanning electron microscopy (SEM) images were obtained using a Carl Zeiss FE-SEM Σigma under an accelerating voltage of 5.00 kV at a facility provided by the Laboratorio de Microscopia Electrónica y Análisis por Rayos X (LAMARX), Córdoba, Argentina.

SERS Measurements. SERS measurements were performed using a Horiba LabRaman confocal microscope with a 100× (NA = 0.70) objective in the backscattering geometry. The spectra acquisition time was 20 s with a 600 lines mm^{-1} grating, giving a resolution of 4 cm^{-1}. The excitation wavelength used was 633 nm (laser line from He−Ne). All measurements were performed at room temperature and were calibrated to Si.

Computational Methods. The optical responses of Au NSs were computed using the generalized multiparticle Mie theory as described elsewhere.[67−69] In all near-field calculations presented in this work the dielectric function tabulated by Palik for Au was employed.[70] For the GMM calculations of the cluster near-field optical properties a multipolar expansion order of 10 was used. In the calculations performed in this work the NPs were excited by a plane wave with an incidence pointing vector (propagation direction) normal to the surface. The GMM code is restricted to applications in homogeneous media; therefore we have used an effective medium approximation[63] to account for the interface between the cell surface and the aqueous environment. We consider that particles were immersed in a dielectric environment with an effective refractive index of n_{eff} = 1.23, which was calculated as the average between the refractive index of the membrane (nr = 1.45) and air (nr = 1.0003).

REFERENCES AND NOTES

1. Martin, F. L.; Kelly, J. G.; Llabjani, V.; Martin-Hirsch, P. L.; Patel, I. I.; Trevisan, J.; Fullwood, N. J.; Walsh, M. J. Distinguishing Cell Types or Populations Based on the Computational Analysis of their Infrared Spectra. *Nat. Protoc.* **2010**, *5*, 1748–1760.
2. Yi, C.; Liu, D.; Yang, M. Building Nanoscale Architectures by Directed Synthesis and Self-Assembly. *Curr. Nanosci.* **2009**, *5*, 75–87.
3. Fraire, J. C.; Pérez, L. A.; Coronado, E. A. Rational Design of Plasmonic Nanostructures for Biomolecular Detection: Interplay between Theory and Experiments. *ACS Nano* **2012**, *6*, 3441–3452.
4. Gregas, M. K.; Scaffidi, J. P.; Lauly, B.; Vo-Dinh, T. Surface-Enhanced Raman Scattering Detection and Tracking of Nanoprobes: Enhanced Uptake and Nuclear Targeting in Single Cells. *Appl. Spectrosc.* **2010**, *8*, 858–866.
5. Hodges, M. D.; Kelly, j. G.; Bentley, A. J.; Fogarty, S.; Patel, I. I.; Martin, F. L.; Fullwood, N. J. Combining Immunolabeling and Surface-Enhanced Raman Spectroscopy on Cell Membranes. *ACS Nano* **2011**, *5*, 9535–9541.
6. Wang, H. Y.; Rong, G. X.; Yan, B.; Yang, L. L.; Reinhard, B. M. Optical Sizing of Immunolabel Clusters through Multispectral Plasmon Coupling Microscopy. *Nano Lett.* **2011**, *11*, 498–504.
7. Wang, J.; Boriskina, S. V.; Wang, H.; Reinhard, B. M. Illuminating Epidermal Growth Factor Receptor Densities on Filopodia through Plasmon Coupling. *ACS Nano* **2011**, *5*, 6619–6628.
8. Rong, G. X.; Wang, H. Y.; Skewis, L. R.; Reinhard, B. M. Resolving Sub-Diffraction Limit Encounters in Nanoparticle Tracking Using Live Cell Plasmon Coupling Microscopy. *Nano Lett.* **2008**, *8*, 3386–3393.
9. Crow, M. J.; Grant, G.; Provenzale, J. M.; Wax, A. Molecular Imaging and Quantitative Measurement of Epidermal Growth Factor Receptor Expression in Live Cancer Cells Using Immunolabeled Gold Nanoparticles. *Am. J. Roentgenol.* **2009**, *192*, 1021–1028.
10. Aaron, J.; Travis, K.; Harrison, N.; Sokolov, K. Dynamic Imaging of Molecular Assemblies in Live Cells Based on Nanoparticle Plasmon Resonance Coupling. *Nano Lett.* **2009**, *9*, 3612–3618.
11. Austin, L. A.; Kang, B.; Yen, C. W.; El-Sayed, M. A. Plasmonic Imaging of Human Oral Cancer Cell Communities during Programmed Cell Death by Nuclear-Targeting Silver Nanoparticles. *J. Am. Chem. Soc.* **2011**, *133*, 17594–17597.
12. Qian, W.; Huang, X. H.; Kang, B.; El-Sayed, M. A. Dark-Field Light Scattering Imaging of Living Cancer Cell Component from Birth through Division Using Bioconjugated Gold Nanoprobes. *J. Biomed. Opt.* **2010**, *15*, 046025.
13. Seekell, K.; Crow, M. J.; Marinakos, S.; Ostrander, J.; Chilkoti, A.; Wax, A. Hyperspectral Molecular Imaging of Multiple Receptors Using Immunolabeled Plasmonic Nanoparticles. *J. Biomed. Opt.* **2011**, *16*, 116003.
14. Crow, M. J.; Seekell, K.; Ostrander, J. H.; Wax, A. Monitoring of Receptor Dimerization Using Plasmonic Coupling of Gold Nanoparticles. *ACS Nano* **2011**, *5*, 8532–8540.
15. Kennedy, D. C.; Tay, L. L.; Lyn, R. K.; Rouleau, Y.; Hulse, J.; Pezacki, J. P. Nanoscale Aggregation of Cellular β2-Adrenergic Receptors Measured by Plasmonic Interactions of Functionalized Nanoparticles. *ACS Nano* **2009**, *3*, 2329–2339.
16. Wang, J.; Yu, X.; Boriskina, S. V.; Reinhard, B. M. Quantification of Differential ErbB1 and ErbB2 Cell Surface Expression

and Spatial Nanoclustering through Plasmon Coupling. *Nano Lett.* **2011**, *5*, 6619–6628.

17. Hodges, M. D.; Kelly, J. G.; Bentley, A. J.; Fogarty, S.; Patel, I. I.; Martin, F. L.; Fullwood, N. J. Combining Immunolabeling and Surface-Enhanced Raman Spectroscopy on Cell Membranes. *ACS Nano* **2011**, *5*, 9535–9541.

18. Ahijado-Guzmán, R.; Gomez-Puertas, P.; Alvarez-Puebla, R. A.; Rivas, G.; Liz-Marzán, L. M. Surface-Enhanced Raman Scattering-Based Detection of the Interactions between the Essential Cell Division FtsZ Protein and Bacterial Membrane Elements. *ACS Nano* **2012**, *6*, 7514–7520.

19. Fullwood, N. J.; Davies, Y.; Nieduszynski, I. A.; Marcyniuk, B.; Ridgway, A. E.; Quantock, A. J. Cell Surface-Associated Keratan Sulphate on Normal and Migrating Corneal Endothelium. *Invest. Ophthalmol. Vis. Sci.* **1996**, *37*, 1256–1270.

20. Herpers, B.; Xanthakis, D.; Rabouille, C. ISH-IEM: A Sensitive Method to Detect Endogenous mRNAs at the Ultrastructural Level. *Nat. Protoc.* **2010**, *5*, 678–687.

21. Chen, L.; Wei, H.; Guo, Y.; Cui, Z.; Zhang, Z.; Zhang, X. E. Gold Nanoparticle Enhanced Immuno-PCR for Ultrasensitive Detection of Hantaan Virus Nucleocapsid Protein. *J. Immunol. Methods* **2009**, *346*, 64–70.

22. Potu_cková, L.; Franko, F.; Bambousková, M.; Dráber, P. Rapid and Sensitive Detection of Cytokines Using Functionalized Gold Nanoparticle-Based Immuno-PCR, Comparison with Immuno-PCR and ELISA. *J. Immunol. Methods* **2011**, *371*, 38–47.

23. Yang, S.; Raymond-Stintz, M. A.; Ying, W.; Zhang, J.; Lidke, D. S.; Steinberg, S. L.; Williams, L.; Oliver, J. M.; Wilson, B. S. Mapping ErbB Receptors on Breast Cancer Cell Membranes during Signal Transduction. *J. Cell Sci.* **2007**, *120*, 2763–2773.

24. Lessard, A.; Coleman, C. G.; Pickel, V. M. Chronic Intermittent Hypoxia Reduces Neurokinin-1 (NK1) Receptor Density in Small Dendrites of Non-catecholaminergic Neurons in Mouse Nucleus Tractus Solitarius. *Exp. Neurol.* **2010**, *223*, 634–644.

25. Stump, R. F.; Pfeiffer, J. R.; Seagrave, J.; Oliver, J. M. Mapping Gold-Labeled IgE Receptors on Mast Cells by Scanning Electron Microscopy: Receptor Distributions Revealed by Silver Enhancement, Backscattered Electron Imaging, and Digital Image Analysis. *J. Histochem. Cytochem.* **1988**, *36*, 493–503.

26. Crow, M. J.; Grant, G.; Provenzale, J. M.; Wax, A. Molecular Imaging and Quantitative Measurement of Epidermal Growth Factor Receptor Expression in Live Cancer Cells Using Immunolabeled Gold Nanoparticles. *AJR Am. J. Roentgenol.* **2009**, *192*, 1021–1028.

27. Kelly, K. L.; Coronado, E. A.; Zhao, L. L.; Schatz, G. C. The Optical Properties of Metal Nanoparticles: The Influence of Size, Shape, and Dielectric Environment. *J. Phys. Chem. B* **2003**, *107*, 668–677.

28. Perassi, E. M.; Hernandez-Garriddo, J. C.; Moreno, M. S.; Encina, E. R.; Coronado, E. A.; Midgley, P. A. Using Highly Accurate 3D Nanometrology to Model the Optical Properties of Highly Irregular Nanoparticles: A Powerful Tool for Rational Design of Plasmonic Devices. *Nano Lett.* **2010**, *10*, 2097–2104.

29. Kambhampati, P.; Child, C. M.; Foster, M. C.; Campion, A. On the Chemical Mechanism of Surface Enhanced Raman Scattering: Experiment and Theory. *J. Chem. Phys.* **1998**, *108*, 5013–5026.

30. Li, S.; Pedano, M. L.; Chang, S.-H.; Mirkin, C. A.; Schatz, G. C. Gap Structure Effects on Surface-Enhanced Raman Scattering Intensities for Gold Gapped Rods. *Nano Lett.* **2010**, *10*, 1722–1727.

31. Su, K. H.; Wei, Q. H.; Zhang, X.; Mock, J. J.; Smith, D. R.; Schultz, S. Interparticle Coupling Effects on Plasmon Resonances of Nanogold Particles. *Nano Lett.* **2003**, *3*, 1087–1090.

32. Jiang, J.; Bosnick, K.; Maillard, M.; Brus, L. Single Molecule Raman Spectroscopy at the Junctions of Large Ag Nanocrystals. *J. Phys. Chem. B* **2003**, *107*, 9964–9972.

33. Gunnarsson, L.; Bjerneld, E. J.; Xu, H.; Petronis, S.; Kasemo, B.; Kall, M. Interparticle Coupling Effects in Nanofabricated Substrates for Surface-Enhanced Raman Scattering. *Appl. Phys. Lett.* **2001**, *78*, 802–804.

34. Jain, P. K.; El-Sayed, M. A. Surface Plasmon Coupling and Its Universal Size Scaling in Metal Nanostructures of Complex Geometry: Elongated Particle Pairs and Nanosphere Trimers. *J. Phys. Chem. C* **2008**, *112*, 4954–4960.

35. Rechberger, W.; Hohenau, A.; Leitner, A.; Krenn, J. R.; Lamprecht, B.; Aussenegg, F. R. Optical Properties of Two Interacting Gold Nanoparticles. *Opt. Commun.* **2003**, *220*, 137–141.

36. Xu, H. X.; Aizpurua, J.; Kall, M.; Apell, P. Electromagnetic Contributions to Single-Molecule Sensitivity in Surface-Enhanced Raman Scattering. *Phys. Rev. E* **2000**, *62*, 4318–4324.

37. Prodan, E.; Radloff, C.; Halas, N. J.; Nordlander, P. A Hybridization Model for the Plasmon Response of Complex Nanostructures. *Science* **2003**, *302*, 419–422.

38. Halas, N. J.; Lal, S.; Chang, W. S.; Link, S.; Nordlander, P. Plasmons in Strongly Coupled Metallic Nanostructures. *Chem. Rev.* **2011**, *111*, 3913–3961.

39. Rozengurt, E. J.; Sinnett-Smith, J.; Van Lint, J.; Valverde, A. M. Protein Kinase D (PKD): A Novel Target for Dyacylglycerol and Phorbol Esters. *Mutat. Res.* **2005**, *333*, 153–160.

40. Díaz Añel, A. M.; Malhotra, V. PKCeta Is Required for Beta1gamma2/Beta3gamma2- and PKD-Mediated Transport to the Cell Surface and the Organization of the Golgi Apparatus. *J. Cell Biol.* **2005**, *169*, 83–91.

41. Rozengurt, E. Protein Kinase D Signaling: Multiple Biological Functions in Health and Disease. *Physiology (Bethesda)* **2011**, *26*, 23–33.

42. Díaz Añel, A. M. Phospholipase C Beta3 Is a Key Component in the Gbetagamma/PKCeta/PKD-Mediated Regulation of Trans-Golgi Network to Plasma Membrane Transport. *Biochem. J.* **2007**, *406*, 157–165.

43. Fu, Y.; Rubin, C. S. Protein Kinase D: Coupling Extracellular Stimuli to the Regulation of Cell Physiology. *EMBO Rep.* **2011**, *12*, 785–796.

44. Olayioye, M. A.; Barisic, S.; Hausser, A. Multi-Level Control of Actin Dynamics by Protein Kinase D. *Cell Signal* **2013**, *25*, 1739–1747.

45. Ellwanger, K.; Hausser, A. Physiological Functions of Protein Kinase D in Vivo. *IUBMB Life* **2013**, *65*, 98–107.

46. Bard, F.; Malhotra, V. The Formation of TGN-To-Plasma-Membrane Transport Carriers. *Annu. Rev. Cell Dev. Biol.* **2006**, *22*, 439–455.

47. Malhotra, V.; Campelo, F. PKD Regulates Membrane Fission to Generate TGN to Cell Surface Transport Carriers. *Cold Spring Harb. Perspect. Biol.* **2011**, *3*, a005280.

48. Yeaman, C.; Ayala, M. I.; Wright, J. R.; Bard, F.; Bossard, C.; Ang, A.; Maeda, Y.; Seufferlein, T.; Mellman, I.; Nelson, W. J.; Malhotra, V. Protein Kinase D Regulates Basolateral Membrane Protein Exit From Trans-Golgi Network. *Nat. Cell Biol.* **2004**, *6*, 106–112.

49. Bisbal, M.; Conde, C.; Donoso, M.; Bollati, F.; Sesma, J.; Quiroga, S.; Díaz Añel, A. M.; Malhotra, V.; Marzolo, M. P.; Cáceres, A. Protein Kinase D Regulates Trafficking of Dendritic Membrane Proteins in Developing Neurons. *J. Neurosci.* **2008**, *28*, 9297–9308.

50. Masu, M.; Tanabe, Y.; Tsuchida, K.; Shigemoto, R.; Nakanishi, S. Sequence and Expression of a Metabotropic Glutamate Receptor. *Nature* **1991**, *49*, 760–765.

51. Valenti, O.; Conn, P. J.; Marino, M. J. Distinct Physiological Roles of the Gq-Coupled Metabotropic Glutamate Receptors Co-Expressed in the Same Neuronal Populations. *J. Cell Physiol.* **2002**, *191*, 125–137.

52. Dhami, G. K.; Ferguson, S. S. G. Regulation of Metabotropic Glutamate Receptor Signaling, Desensitization and Endocytosis. *Pharmacol. Ther.* **2006**, *111*, 260–271.

53. Willard, S. S.; Koochekpour, S. Glutamate Signaling in Benign and Malignant Disorders: Current Status, Future Perspectives, and Therapeutic Implications. *Int. J. Biol. Sci.* **2013**, *9*, 728–742.

54. Wang, H.; Rong, G.; Yan, B.; Reinhard, B. M. Optical Sizing of Immunolabel Clusters through Multispectral Plasmon Coupling Microscopy. *Nano Lett.* **2011**, *11*, 498–504.

55. Aaron, J.; Nitin, N.; Travis, K.; Kumar, S.; Collier, T.; Park, S. Y.; Jose-Yacamán, M.; Coghlan, L.; Follen, M.; Richards-Kortum, R.; *et al*. Plasmon Resonance Coupling of Metal Nanoparticles for Molecular Imaging of Carcinogenesis in Vivo. *J. Biomed. Opt.* **2007**, *12*, 034007.

56. Fraire, J. C.; Pérez, L. A.; Coronado, E. A. Cluster Size Effects in the SERS Response of Ag and Au Nanoparticle Aggregates: Experimental and Theoretical Insight. *J. Phys. Chem. C* **2013**, *117*, 23090–23107.

57. Luján, R.; Roberts, J. D. B.; Shigemoto, R.; Ohishi, H.; Somogyi, P. Differential Plasma Membrane Distribution of Metabotropic Glutamate Receptors mGluR1a, mGluR2 and mGluR5, Relative to Neurotransmitter Release Sites. *J. Chem. Neuroanat.* **1997**, *13*, 219–241.

58. Garraleta, B. C.; Norton, P. R.; Lagugné-Labarthet, F. SERS Detection of Streptavidin/Biotin Monolayer Assemblies. *Langmuir* **2011**, *27*, 1494–1498.

59. Ringler, M.; Klar, T. A.; Schwemer, A.; Susha, A. S.; Stehr, J.; Raschke, G.; Funk, S.; Borowski, M.; Nichtl, A.; Kulrzinger, K.; Phillips, R. T.; Feldman, J. Moving Nanoparticles with Raman Scattering. *Nano Lett.* **2007**, *7*, 2753–2757.

60. Barth, A.; Zscherp, C. What Vibrations Tell Us about Proteins. *Q. Rev. Biophys.* **2002**, *35*, 369–430.

61. Le Ru, E.; Etchegoin, P. G. *Principles of Surface Enhanced Raman Spectroscopy*, Vol. 1; Elsevier: Amsterdam, 2009.

62. Moskovits, M. Persistent Misconceptions Regarding SERS. *Phys. Chem. Chem. Phys.* **2013**, *15*, 5301–5311.

63. Tamaru, H.; Kuwata, H.; Miyazaki, H. T.; Miyano, K. Resonant Light Scattering from Individual Ag Nanoparticles and Particle Pairs. *Appl. Phys. Lett.* **2002**, *80*, 1826–1828.

64. Kunda, P.; Paglini, G.; Quiroga, S.; Kosik, K.; Cáceres, A. Evidence for the Involvement of Tiam-1 in Axon Formation. *J. Neurosci.* **2001**, *21*, 2361–2372.

65. Rosso, S.; Bollati, F.; Bisbal, M.; Peretti, D.; Sumi, T.; Nakamura, T.; Quiroga, S.; Ferreira, A.; Cáceres, A. LIMK1 Regulates Golgi Dynamics, Traffic of Golgiderived Vesicles, and Process Extension in Primary Cultured Neurons. *Mol. Biol. Cell* **2004**, *15*, 3433–3449.

66. Jeyifous, O.; Waites, C. L.; Specht, C. G.; Fujisawa, S.; Schubert, M.; Lin, E. I.; Marshall, J.; Aoki, C.; de Silva, T.; Montgomery, J. M.; *et al*. SAP97 and CASK Mediate Sorting of NMDA Receptors through a Previously Unknown Secretory Pathway. *Nat. Neurosci.* **2009**, *12*, 1011–1019.

67. Encina, E. R.; Coronado, E. A. On the Far Field Optical Properties of Ag—Au Nanosphere Pairs. *J. Phys. Chem. C* **2010**, *114*, 16278–16284.

68. Encina, E. R.; Coronado, E. A. Plasmon Coupling in Silver Nanosphere Pairs. *J. Phys. Chem. C* **2010**, *114*, 3918–3923.

69. Encina, E. R.; Coronado, E. A. Near Field Enhancement in Ag Au Nanospheres Heterodimers. *J. Phys. Chem. C* **2011**, *115*, 15908–15914.

70. Palik, E. D. *Handbook of Optical Constants of Solids*; Academic Press: New York, 1985.